Chemical Science

ROYAL SOCIETY OF CHEMISTRY

EDGE ARTICLE

View Article Online
View Journal

Check for updates

Cite this: DOI: 10.1039/d5sc09439a

All publication charges for this article have been paid for by the Royal Society of Chemistry

Open Access Article. Published on 16 February 2026. Downloaded on 4/13/2026 7:48:14 AM. This article is licensed under a Creative Commons Attribution-NonCommercial 3.0 Unported Licence.

# Achieving switchable UV/Vis circularly polarized luminescence by varying excitation wavelength in chiral indium halides

Xin-Ping Guo,[abc] Hao-Wei Lin,[ad] Abdusalam Ablez,[abc] Sheng-Mao Zhang,[e] Yu-Wei Ren,[abc] Guo-Yang Chen,[abc] Wei-Yu Zhang,[abc] Ke-Zhao Du, *[e] Ze-Ping Wang *[a] and Xiao-Ying Huang *[acd]

Chiral organic-inorganic hybrid metal halides (OIMHs) are promising for dynamic circularly polarized luminescence (CPL) in next-generation photonics. However, the dynamic switching of CPL signals across different emission regions, especially across the scarce ultraviolet (UV) region, remains a significant challenge. Herein, we report a pair of chiral indium halide enantiomers, (*R*/*S*-$MPH_2$)[$InCl_4$(2,2′-bpy)]Cl (***R*/*S*-1**, MP = 2-methylpiperazine, 2,2′-bpy = 2,2′-bipyridine), synthesized by leveraging the diverse coordination geometry of the $In^{3+}$ ion and its balanced binding affinity for both halogens and organic ligands. Through the strategic incorporation of the UV-emissive 2,2′-bpy ligand and chiral blue-emissive $(R/S\text{-}MPH_2)^{2+}$ cation, ***R*/*S*-1** achieves reversible luminescence switching between the UV region (peaking at 345 nm) and visible (Vis) region (peaking at 460 nm). More importantly, effective chirality transfer, mediated through hydrogen bonding, enables CPL activity at these wavelengths with excitation-dependent characteristics. This system demonstrates the first reversible switching of CPL emission between the UV and visible regions in OIMHs. Notably, the CPL switching system also exhibits a large luminescence asymmetry factor ($g_{lum}$) in the UV region ($\sim 10^{-1}$), a value about 30-fold greater than that of the emission in the visible region. The practical potential of switchable circularly polarized light is demonstrated through the construction of a chiral photonic logic gate and a subsequent anti-counterfeiting system based on Morse code. This work offers a viable design strategy for dynamically tunable CPL materials while demonstrating the promise of such materials for advanced applications in information security.

Received 3rd December 2025
Accepted 15th February 2026

DOI: 10.1039/d5sc09439a

rsc.li/chemical-science

## Introduction

Circularly polarized luminescence (CPL) materials have garnered significant research interest due to their promising applications in advanced technologies such as three-dimensional (3-D) displays,[1] data storage,[2] and biomedicine.[3] The performance of these materials is intrinsically linked to their emission regions. For instance, ultraviolet (UV, 10–400 nm) CPL (UV-CPL), with its high photon energy and resolution, is an ideal polarized source for stereoselective photopolymerization.[4–6] Visible (Vis, 400–780 nm) CPL (Vis-CPL) holds great potential in 3-D displays, bioimaging, and information encryption,[7–10] while near-infrared (NIR, 780–2500 nm) CPL (NIR-CPL) has garnered significant interest for applications like early tumour detection and information security, owing to its deep tissue penetration and low visibility compared to visible light.[11,12] This region-function correlation has fuelled the pursuit of materials with switchable CPL emissions. Realizing multi-region CPL switching within a single material system represents a streamlined approach to multifunctionality, circumventing the need for laborious synthesis of multiple discrete materials.[13] A central challenge in this field lies in the integrated control of the chiral environment and the stimuli-responsive reversible switching of CPL across multiple luminescent centres.[13] A major obstacle is that stimuli-responsive structural transformations frequently cause chiral elimination, leading to the disappearance of the CPL signal.[14]

Chiral organic-inorganic hybrid metal halides (OIMHs) have recently garnered significant attention as a new class of CPL-active materials.[15–18] The tunability in their structure and composition enables the optimization of CPL performance through chiral cation modification and component

[a]State Key Laboratory of Structural Chemistry, Fujian Institute of Research on the Structure of Matter, Chinese Academy of Sciences, Fuzhou, 350002, P. R. China. E-mail: xyhuang@fjirsm.ac.cn; wzping520@msn.cn

[b]College of Chemistry, Fuzhou University, Fuzhou 350108, P. R. China

[c]Fujian College, University of Chinese Academy of Sciences, Fuzhou 350002, P.R. China

[d]University of Chinese Academy of Sciences, Beijing 100049, P. R. China

[e]Fujian Provincial Key Laboratory of Advanced Materials Oriented Chemical Engineering, Fujian Normal University, Fuzhou 350007, P. R. China. E-mail: dkz007002@163.com

© 2026 The Author(s). Published by the Royal Society of Chemistry

Open Access Article. Published on 16 February 2026. Downloaded on 4/13/2026 7:48:14 AM. This article is licensed under a Creative Commons Attribution-NonCommercial 3.0 Unported Licence.

engineering.[19–30] Owing to their highly tuneable structures and compositions, chiral OIMHs have emerged as promising candidates with switchable CPL regions.[31] Current research on reversible CPL switching of OIMHs is mostly through external stimuli such as protonation states,[32] temperature,[33] or solvents.[34] The stimuli-responsive CPL switching is associated with structural transformations induced by chemical reactions. By contrast, excitation-dependent CPL switching controls emission by adjusting the excitation wavelength without inducing structural changes, thereby exhibiting outstanding structural integrity. Furthermore, this method offers the combined advantages of operational simplicity, excellent reversibility, and low cost.[35–37] Nevertheless, research on excitation-dependent CPL materials remains in its early stages,[38] and most reported materials exhibit only a slight shift in the visible region, rather than a switching across UV-Vis-NIR spectral regions.

The introduction of organic ligands provides a powerful approach for tuning the properties of hybrid metal halides by modifying their inorganic anion components or introducing additional functional organic component.[39,40] Guided by this strategy, the main-group metal $In^{3+}$ was selected as the central ion in this study due to its diverse coordination geometries and balanced affinity for both halides and organic ligands. By coordinating UV-emissive organic ligand 2,2′-bipyridine (2,2′-bpy) and chiral blue-emissive $(R/S\text{-MPH}_2)^{2+}$ (MP = 2-methylpiperazine) cations, a pair of chiral hybrid indium halide enantiomers of $(R/S\text{-MPH}_2)[\text{In Cl}_4(2,2'\text{-bpy})]\text{Cl}$ (denoted as ***R*/*S*-1**) were successfully constructed. Their crystal structures and photophysical properties were subsequently investigated in detail, demonstrating effective regulation of the material's CPL. These compounds exhibit distinct CPL signals at 345 nm (UV region) and 460 nm (Vis region). To our knowledge, ***R*/*S*-1** represents the first example of main-group metal-based chiral hybrid materials exhibiting UV CPL. Furthermore, reversible switching of the CPL emission between the UV and visible regions was readily achieved in ***R*/*S*-1** by simply altering the excitation wavelength. The practical utility of this material was also demonstrated in applications such as anti-counterfeiting and chiral logic gates. This study, therefore, establishes a novel structural design paradigm for the development of advanced chiroptical materials.

## Results and discussion

### Crystal structure and stability

Compounds $(R/S\text{-MPH}_2)[\text{InCl}_4(2,2'\text{-bpy})]\text{Cl}$ (***R*/*S*-1**) were prepared as a pair of zero-dimensional (0D) chiral indium chloride enantiomers *via* solvent evaporation from a solution of *R*/*S*-MP, $\text{In Cl}_3\cdot 4\text{H}_2\text{O}$, and 2,2′-bpy in a mixed hydrochloric acid/acetonitrile solvent (see the SI for details). Crystallographic data are summarized in Table S1 (SI).

Single-crystal X-ray diffraction reveals that ***R*/*S*-1** crystallizes in the triclinic chiral space group *P*1. The asymmetric unit comprises two $[\text{In Cl}_4(2,2'\text{-bpy})]^-$ anions, two chiral cations $(R/S\text{-MPH}_2)^{2+}$, and two chloride ions (Fig. 1a). The spatial arrangements of the cationic and anionic components along the *bc* plane illustrate the mirror-symmetric relationship between the *R*- and *S*-enantiomers (Fig. 1b). The crystal structure is further stabilized by forming an extensive three-dimensional (3D) hydrogen-bonding network (Fig. S2). Additionally, π···π interactions are observed between the pyridine rings of adjacent anions, as denoted by the yellow dashed lines in Fig. S3.

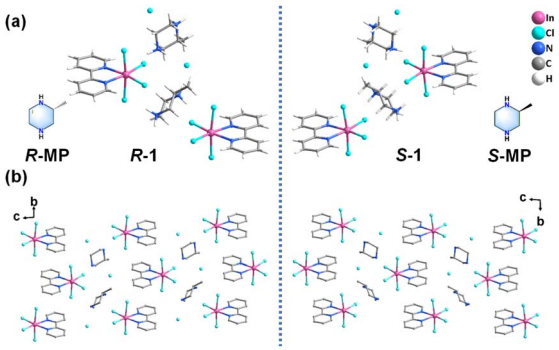


Fig. 1 (a) Asymmetric units of ***R*/*S*-1**. The molecular structures of *R*/*S*-MP are also shown. (b) Spatial arrangement of the cationic and anionic components in the crystal structures of ***R*/*S*-1**, projected onto the *bc* plane. Hydrogen atoms are omitted for clarity.

Experimental powder X-ray diffraction (PXRD) patterns of ***R*/*S*-1** match well with the simulated ones from the single-crystal data, confirming the phase purity of the bulk samples (Fig. S4). Thermogravimetric analysis (TGA) indicates that ***R*/*S*-1** exhibits no decomposition below 230 °C (Fig. S5).

### Optical absorption and DFT calculations

As shown in Fig. 2a, the solid-state UV-Vis absorption spectra of ***R*/*S*-1** span 200–350 nm. Their transmission on the visible light range is consistent with the colourless appearance. Density functional theory (DFT) calculations are performed on compound ***R*-1** to further understand the optical properties. The

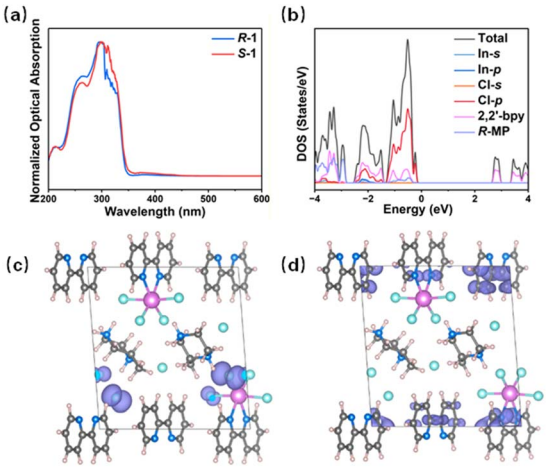


Fig. 2 (a) UV-Vis absorption spectra of ***R*/*S*-1**. (b) The diagram of density of states (DOSs) for ***R*-1**. Molecular orbitals of ***R*-1** showing the highest occupied molecular orbital (HOMO) (c), and the lowest occupied molecular orbital (LUMO) (d).


© 2026 The Author(s). Published by the Royal Society of Chemistry

Open Access Article. Published on 16 February 2026. Downloaded on 4/13/2026 7:48:14 AM. This article is licensed under a Creative Commons Attribution-NonCommercial 3.0 Unported Licence.

computational data demonstrate that ***R*-1** is a direct bandgap semiconductor with a bandgap value of 2.928 eV, which is slightly smaller than the bandgap value (3.644 eV) experimentally determined from the UV-Vis absorption spectrum (Fig. S6). This discrepancy arises from the insufficient precision of the GGA in characterising the eigenvalues of the electronic states.[41,42] The density of states (DOSs) in Fig. 2b shows that the valence band maximum (VBM) is mainly contributed by the 3p orbital of Cl, while the conduction band minimum (CBM) is primarily contributed by 2,2′-bpy. This indicates a charge transfer between the Cl 3p orbitals and the organic ligand in the absorption process of ***R*-1**. The difference between the sum of p-state density and the total density of states in DOSs is derived from the Wigner-Seitz radius division of the Vienna *Ab initio* Simulation Package (VASP) in this DFT calculation. The radius chosen in this partitioning method fails to cover the entire lattice, and the partitions are not additive.[43,44] Consequently, the calculated total p-state density is always less than the total DOSs. Molecular orbital calculations were performed to elucidate the electronic structure. As shown in Fig. 2c, the highest occupied molecular orbital (HOMO) of ***R*-1** is predominantly localized on the p orbital of the Cl4 atom coordinated to the In (2) centre, exhibiting a spindle-shaped electron density distribution. By contrast, the lowest unoccupied molecular orbital (LUMO) is characterized by a peanut-shaped π electron cloud primarily residing on the pyridine ring of the 2,2′-bpy ligand (Fig. 2d).

## Photoluminescence

Under 365 nm UV light irradiation, both ***R*-1** and ***S*-1** enantiomers exhibit blue fluorescence. Their luminescence properties were investigated through photoluminescence (PL), photoluminescence excitation (PLE), and time-resolved PL spectroscopy, with key optical parameters summarized in Table 1. It is revealed that ***R*/*S*-1** exhibits PL in both the UV and visible wavelength regions. When excited at approximately 280 nm at 300 K, a UV emission region centred at 345 nm is observed (Fig. 3a and b). When excited at 355 nm, however, a visible emission region emerges with a peak at 460 nm (Fig. 3c and d).

The luminescence origins of the ***R*/*S*-1** enantiomers were then elucidated by investigating the intrinsic photophysical properties of the pristine 2,2′-bpy ligand and *R*/*S*-MP. The free 2,2′-bpy ligand exhibits a high-energy emission region at 364 nm when excited at 280 nm (Fig. S7a). In ***R*/*S*-1**, this region is blue-shifted to 345 nm, an effect attributed to the enhanced structural rigidity upon coordination of 2,2′-bpy to the $In^{3+}$ centre. This assignment is consistent with UV emission features reported for other coordination complexes containing 2,2′-bpy and its derivatives.[45–49] Separately, *R*/*S*-MP displays a visible emission region around 460 nm under 380 nm excitation (Fig. S7b), which might contribute to the 460 nm emission peak of ***R*/*S*-1**. The distinct emissive states of these components are directly linked to the switchable CPL behaviour observed in ***R*/*S*-1**. In ***R*/*S*-1**, the UV emission at 345 nm exhibits a short lifetime of approximately 0.8 ns (Fig. 3e), whereas the visible emission at 460 nm exhibits a significantly longer lifetime of approximately 3 ns (Fig. 3f). Furthermore, the photoluminescence quantum yield (PLQY) for the visible emission (13.15% for ***R*-1** and 9.56% for ***S*-1**, respectively) is markedly higher than that for the UV emission (5.27% for ***R*-1** and 5.90% for ***S*-1**, respectively). The lower efficiency of the UV emission likely results from enhanced non-radiative decay pathways, potentially due to the self-absorption effect verified by the overlap between the optical absorption and UV emission.

Based on theoretical calculations, spectroscopic data, and existing literature on hybrid metal halides, the luminescence mechanism of ***R*/*S*-1** is proposed as follows: the UV emission at 345 nm is assigned to the singlet transition of the 2,2′-bpy ligand, whereas the visible emission at 460 nm originates from a singlet transition of the *R*/*S*-MP component. This distinct origin of the two emissions enables the observed excitation-dependent emission spectra of ***R*/*S*-1**. As shown in Fig. S8, while excitation between 250 and 320 nm results in a maximum emission at 345 nm (characteristic of the UV channel), red-shifting the excitation to 330–390 nm shifts the dominant PL peak to 460 nm, thereby activating the visible channel. These results demonstrate that the emission can be switched between UV and Vis regions solely by controlling the excitation wavelength. Furthermore, the temperature-dependent PL spectra of the visible emission at 460 nm were investigated. The emission intensity exhibits a significant enhancement with decreasing temperature (Fig. S9). This enhancement is attributed to the suppression of non-radiative transition rates at lower temperatures. Concurrently, the emission maximum undergoes a red-shift with increasing temperature, a trend likely induced by enhanced electron-phonon coupling.[39,40]

Table 1 Summary of optical properties of *R*/*S*-1

| Compound | ***R*-1** | | ***S*-1** | |
|---|---|---|---|---|
| $\lambda_{ex}$ (nm) | 280 | 355 | 275 | 355 |
| $\lambda_{em}$ (nm) | 345 | 460 | 345 | 460 |
| Lifetime (ns) | 0.819 | 3.03 | 0.766 | 3.20 |
| PLQY (%) | 5.27 | 13.6 | 5.90 | 9.56 |
| $\lvert g_{lum}\rvert$ ($10^{-3}$) | 120 | 4.00 | 86.0 | 3.00 |

## Chiroptical properties

The chiroptical properties of ***R*/*S*-1** were studied by circular dichroism (CD) spectroscopy. As shown in Fig. S10, the enantiomers exhibit clear mirror-imaged CD signals within the 250–400 nm region, demonstrating good correspondence with their UV absorption profile. Analysis of the chiral origin reveals that hydrogen-bonding interactions between the organic $(R/S\text{-}MPH_2)^{2+}$ cations and the inorganic anions (Fig. S11) serve as the key structural pathway for chiral induction. This interpretation is further corroborated by a comparison of the CD spectra of ***R*/*S*-1** with those of the free *R*/*S*-MP. While the CD signals of pure *R*/*S*-MP are primarily located below 250 nm,[33] those of ***R*/*S*-1** appear in the 250–400 nm range. These results confirm the successful transfer of chirality from the organic cations to the entire hybrid framework.

Open Access Article. Published on 16 February 2026. Downloaded on 4/13/2026 7:48:14 AM.
This article is licensed under a Creative Commons Attribution-NonCommercial 3.0 Unported Licence.

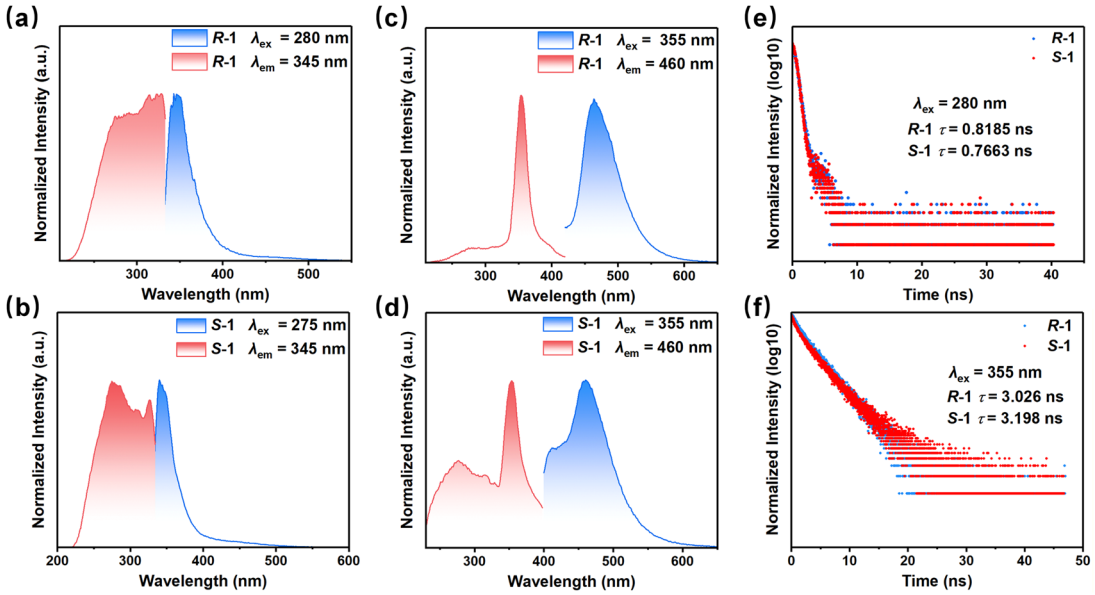


Fig. 3 Excitation and emission spectra of (a) *R*-1 and (b) *S*-1 for the UV emission, and (c) *R*-1 and (d) *S*-1 for the Vis emission, respectively. (e) PL decay curves of *R*/*S*-1 under 280 nm excitation. (f) PL decay curves of *R*/*S*-1 under 355 nm excitation.

To further investigate the chiral transfer during the emission process, the CPL spectra of ***R***/***S*-1** were measured at room temperature. Both enantiomers exhibit mirror-symmetric CPL signals. Under 280 nm excitation, the CPL signal appears in the 320–400 nm range with a maximum at approximately 345 nm (Fig. 4a), consistent with the intrinsic UV emission of the ligand. When excited at 365 nm, the CPL signal covers 420–550 nm and peaks at approximately 460 nm (Fig. 4b), matching the visible emission region. The DC voltage recorded during the CPL measurements is shown in Fig. 4c and d, with the position of its curve corresponding to that of the respective emission peak. The asymmetry of CPL emission is quantified by the luminescence asymmetry factor ($g_{lum}$), where $g_{lum} = 2 \times (I_L - I_R)/(I_L + I_R)$. Here, $I_L$ and $I_R$ represent the intensity of left and right polarized light, respectively.[3,50] As shown in Fig. 4e and f, the $g_{lum}$ values of ***R*-1** and ***S*-1** at 345 nm are 0.12 and −0.086, respectively. By contrast, the $g_{lum}$ values of ***R*-1** and ***S*-1** at 460 nm are $-3 \times 10^{-3}$ and $4 \times 10^{-3}$, respectively, further reflecting the mirror image relationship between enantiomers. To ensure reliable CPL measurements, potential interference

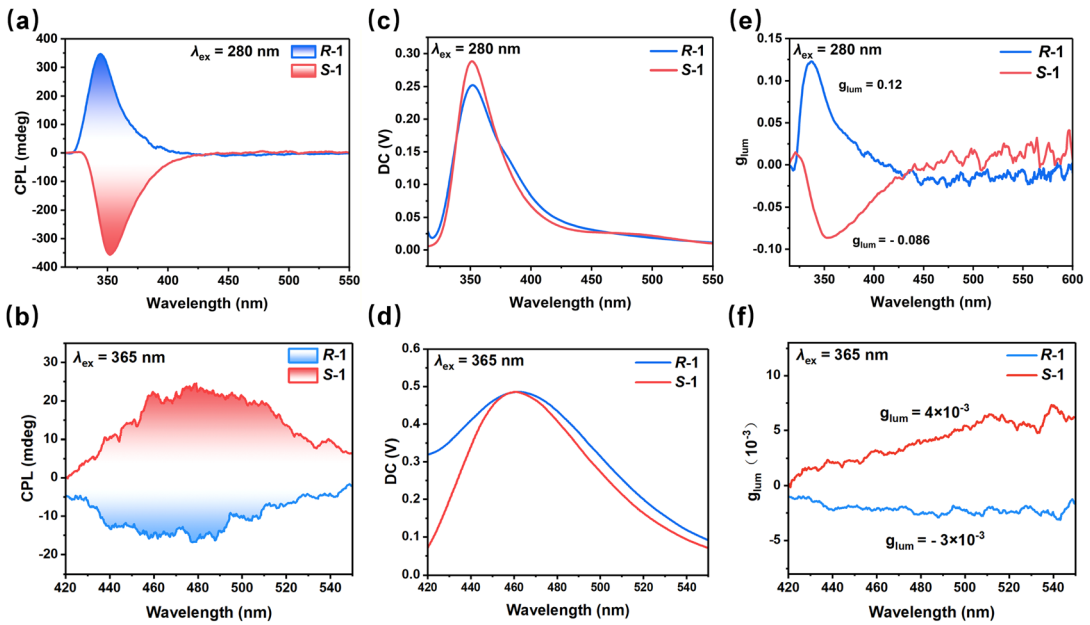


Fig. 4 (a) Circularly polarized spectra of *R*/*S*-1 excited at 280 nm. (b) Circularly polarized spectra of *R*/*S*-1 excited at 365 nm. DC diagrams of *R*/*S*-1 for the CPL spectra under (c) 280 nm and (d) 365 nm excitation. (e) Luminescence dissymmetry factor values of *R*/*S*-1 at different wavelengths under 280 nm excitation. (f) Luminescence dissymmetry factor values of *R*/*S*-1 at different wavelengths under 365 nm excitation.


© 2026 The Author(s). Published by the Royal Society of Chemistry

Open Access Article. Published on 16 February 2026. Downloaded on 4/13/2026 7:48:14 AM.
This article is licensed under a Creative Commons Attribution-NonCommercial 3.0 Unported Licence.

(a)

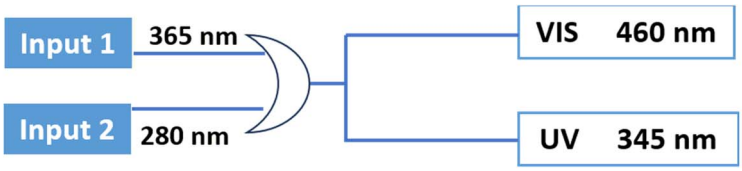


(b)

| Input | | Output | |
|---|---|---|---|
| Input 1 (365 nm) | Input 2 (280 nm) | Output 1 (460 nm) | Output 2 (345 nm) |
| 0 | 0 | 0 | 0 |
| 1 | 0 | 1 | 0 |
| 0 | 1 | 0 | 1 |

(c)

| Morse Code | Letter | Morse Code | Letter | Morse Code | Letter |
|---|---|---|---|---|---|
| —••• | B | •• | I | •—• | R |
| —•—• | C | •——— | J | ••• | S |
| ••—• | F | —— | M | | |

(d)

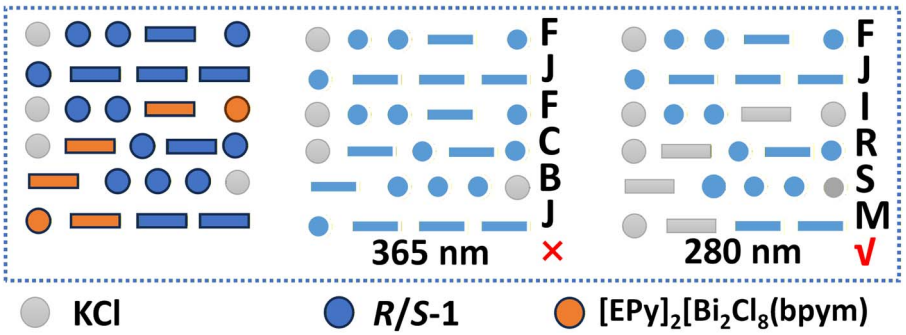


Fig. 5 (a) Schematic diagram of the designed chiral logic gate, and (b) the corresponding truth table. (c) Digital information corresponding to Morse code. (d) Schematic diagram of the digital information encryption process based on Morse code.

from crystal anisotropy and linear polarization was minimized by using small crystals.[19] The reproducibility was further verified by testing multiple independent synthesis batches. High consistency was observed in both the CPL spectra and the corresponding $g_{lum}$ across all batches (Fig. S11 and S12), confirming the intrinsic chiroptical origin of the signals. The $|g_{lum}|$ of the UV emission is 30 times larger than that of its Vis counterpart. This significant difference accounts for the higher PLQY of the visible emission, consistent with the inherent competition between $g_{lum}$ and PLQY in CPL systems.[51] As shown in Table S8, among chiral OIMHs exhibiting emission switching properties, ***R*/*S*-1** is the first material to achieve CPL switching between different emission regions *via* excitation wavelength. Simultaneously, it is also the first chiral OIMH based on main-group metal to successfully realize UV-CPL. This study provides new insights for designing switchable circularly polarized luminescent materials.

### Anti-counterfeiting encryption based on chiral logic gates

Based on the switchable CPL characteristics of ***R*/*S*-1**, its potential as a chiroptical logic element was investigated. Within the constructed logic framework (Fig. 5a), two specific excitation wavelengths (365 nm and 280 nm) are defined as the inputs, with their presence and absence represented by '1' and '0', respectively. The outputs are the CPL signals, specifically defined as Output 1 (visible emission at 460 nm) and Output 2 (UV emission at 345 nm). The output signals are dynamically controlled by modulating the input combinations. The truth table in Fig. 5b lists the output states for all input combinations. The logic gate evaluates to TRUE only when the system sequentially produces output pairs '10' and '01' under two distinct excitations. In this context, the TRUE state is specifically defined by the presence of a '1' in both output pairs. If this condition is not met, the output is FALSE.

Furthermore, an information encryption and anti-counterfeiting system was constructed based on this strategy. The target digital information was first encoded into Morse

Open Access Article. Published on 16 February 2026. Downloaded on 4/13/2026 7:48:14 AM. This article is licensed under a Creative Commons Attribution-NonCommercial 3.0 Unported Licence.

code (Fig. 5c). An array-based encryption pattern was then fabricated (Fig. 5d), in which selected positions were filled with the switchable CPL-active compound ***R*/*S*-1** or the visible-light-emitting yet CPL-inactive compound $[EPy]_2[Bi_2Cl_8(bpym)]$ (EPy = *N*-ethylpyridinium; bpym = 2,2′-bipyrimidine);[52] the remaining areas were filled with non-luminescent KCl powder. Under 365 nm excitation, the system displays the interference message "FJFCBJ", whereas under 280 nm excitation, the true encrypted information "FJIRSM" is revealed. The distinct CPL property of ***R*/*S*-1** allows for authentication *via* polarization detection, thereby establishing a dual-encryption mechanism based on both excitation wavelength and circular polarization. This two-level security strategy significantly enhances the system's anti-counterfeiting robustness.

## Conclusions

In summary, we have successfully synthesized a pair of chiral indium halide enantiomers, ***R*/*S*-1**, by leveraging the diverse coordination geometry of the $In^{3+}$ ion and its balanced binding affinity for both halogens and organic ligands. The UV-emissive 2,2′-bipyridine ligand combined with the blue-emissive *R*/*S*-MP endow ***R*/*S*-1** with switchable luminescent centres between the UV region and visible region. The chirality transfer within the structure through hydrogen bonding interaction makes ***R*/*S*-1** exhibit excitation-dependent CPL. The reversible switching of CPL emission between 345 nm in the UV and 460 nm in the Vis region has not been reported before in OIMHs, which exhibit scarce UV CPL properties. Notably, the $g_{lum}$ in the UV region reaches an order of $10^{-1}$, which is 30 times larger than that of the visible emission. We further demonstrated the practical potential of these switchable CPL characteristics in applications such as anti-counterfeiting using chiroptical logic gates and Morse code. This study not only presents an effective molecular-level strategy for achieving dynamically tuneable CPL but also opens new avenues for the application of chiral materials in advanced photonic technologies.

## Author contributions

X. P. G. and X. Y. H. conceived the project. X. P. G. designed and conducted most of the experiments. A. A. A. and S. M. Z. performed DFT calculations and analysed the data. X. P. G. conducted PL, PLE, PL decay, TG, UV-Vis, XRD, CD, and CPL experiments. W. Y. Z. provided assistance with the synthesis of the compounds. Y. W. R. and G. Y. C. assisted in the preparation of the crystal structure diagrams. X. P. G. prepared the manuscript. X. P. G., H. W. L., Z. P. W., K. Z. D., and X. Y. H. revised the manuscript. All authors discussed the results and provided feedback on the manuscript. X. Y.H. supervised the project.

## Conflicts of interest

There are no conflicts to declare.

## Data availability

CCDC 2488488 and 2488489 contain the supplementary crystallographic data for this paper.[53a,b]

Supplementary information (SI): Experimental section, more figures for PXRD, TG, optical properties, and crystallographic data tables. See DOI: https://doi.org/10.1039/d5sc09439a.

## Acknowledgements

This work was supported by the National Natural Science Foundation of China (Nos. 92261115, 22205236, and 22373014). The DFT calculations in this study were carried out on the Big Earth Data Cloud Service Platform.

## References

1 Y. Liu, Y. Wei, Z. Luo, B. Xu, M. He, P. Hong, C. Li and Z. Quan, *Chem. Sci.*, 2024, **15**, 15480–15488.
2 L. E. MacKenzie and R. Pal, *Nat. Rev. Chem.*, 2020, **5**, 109–124.
3 X. Yang, X. Gao, Y.-X. Zheng, H. Kuang, C.-F. Chen, M. Liu, P. Duan and Z. Tang, *CCS Chem.*, 2023, **5**, 2760–2789.
4 L. Xu, H. Liu, X. Peng, P. Shen, B. Z. Tang and Z. Zhao, *Angew. Chem., Int. Ed.*, 2023, **62**, e202300492.
5 F. Zinna, C. Resta, S. Abbate, E. Castiglioni, G. Longhi, P. Mineo and L. Di Bari, *Chem. Commun.*, 2015, **51**, 11903–11906.
6 Y. Wei, C. Zhong, Y. Sun, S. Ma, M. Ni, X. Wu, Y. Yan, L. Yang, I. A. Khodov, J. Ge, Y. Li, D. Lin, Y. Wang, Q. Bao, H. Zhang, S. Wang, J. Song, J. Lin, L. Xie and W. Huang, *Nat. Commun.*, 2024, **15**, 5438.
7 M. P. Davydova, L. Meng, M. I. Rakhmanova, I. Y. Bagryanskaya, V. S. Sulyaeva, H. Meng and A. V. Artem'ev, *Adv. Opt. Mater.*, 2023, **11**, 2202811.
8 H. L. Xuan, J. L. Li, L. J. Xu, D. S. Zheng and Z. N. Chen, *Adv. Opt. Mater.*, 2022, **10**, 2200591.
9 H. L. Xuan, Y. F. Sang, L. J. Xu, D. S. Zheng, C. M. Shi and Z. N. Chen, *Chem. Eur J.*, 2022, **28**, e202201299.
10 C.-M. Shi, H. Lu, J.-Y. Wang, G. Long, L.-J. Xu and Z.-N. Chen, *Nat. Commun.*, 2025, **16**, 1505.
11 B. Yang, X. Yang, Y. Shi, X. Jin, T. Li, M. Liu and P. Duan, *Angew. Chem., Int. Ed.*, 2024, **64**, e202417223.
12 Y. Huang, Y. Zhou, X. Guo, Z. Tong and T. Zhuang, *Nanoscale*, 2025, **17**, 1922–1931.
13 M. Pan, G. Zhang, H. Ma, X. Cheng, J. Li and W. Zhang, *Sci. China Chem.*, 2024, **67**, 2362–2372.
14 X. Wang, Q. Song, Z. He, G. Zhang, T. Miao, X. Cheng and W. Zhang, *Chin. Chem. Lett.*, 2025, **36**, 110047.
15 Z. Song, B. Yu, G. Liu, L. Meng and Y. Dang, *J. Phys. Chem. Lett.*, 2022, **13**, 2567–2575.
16 S. Liu, X. Wang, Y. Dou, Q. Wang, J. Kim, C. Slebodnick, Y. Yan and L. Quan, *J. Am. Chem. Soc.*, 2024, **146**, 11835–11844.
17 Z. Guo, J. Li, R. Chen and T. He, *Prog. Quant. Electron.*, 2022, **82**, 100375.


© 2026 The Author(s). Published by the Royal Society of Chemistry

Open Access Article. Published on 16 February 2026. Downloaded on 4/13/2026 7:48:14 AM. This article is licensed under a Creative Commons Attribution-NonCommercial 3.0 Unported Licence.

18 Y. Fan, P. Wang, C. Chen, X. Ji, F. Chang and L. Mao, *Sci. China Chem.*, 2025, **68**, 4160–4171.
19 J. Chen, S. Zhang, X. Pan, R. Li, S. Ye, A. K. Cheetham and L. Mao, *Angew. Chem., Int. Ed.*, 2022, **61**, e202205906.
20 J. L. Qi, Y. Guo, J. Wu, Q. F. Huang, J. J. Xu, S. F. Yan, W. Liu and S. P. Guo, *Angew. Chem., Int. Ed.*, 2024, **63**, e202407074.
21 T. Song, C. Q. Wang, H. Lu, X. J. Mu, B. L. Wang, J. Z. Liu, B. Ma, J. Cao, C. X. Sheng, G. Long, Q. Wang and H. L. Zhang, *Angew. Chem., Int. Ed.*, 2024, **63**, e202400769.
22 Y. Wei, C. Li, Y. Li, Z. Luo, X. Wu, Y. Liu, L. Zhang, X. He, W. Wang and Z. Quan, *Angew. Chem., Int. Ed.*, 2022, **61**, e202212685.
23 J. Y. Yao, Q. R. Ding, H. Zeng, J. Y. Wang, C. M. Shi, L. J. Xu and Z. N. Chen, *Angew. Chem., Int. Ed.*, 2025, **64**, e202502099.
24 L. Zhai, J. Yuan, J. Huang, X. W. Pan, L. Wan, W. Ning and X. M. Ren, *Angew. Chem., Int. Ed.*, 2025, **64**, e202425543.
25 Y. Zhang, Y. Wei, C. Li, Y. Wang, Y. Liu, M. He, Z. Luo, X. Chang, X. Kuang and Z. Quan, *Chem. Commun.*, 2025, **61**, 85–88.
26 F. Wang, X. Li, T. Chen, L. Wang, C. Li, W. Zhang, W. Yuan, S. Lu, L. Li and X. Chen, *Chem. Sci.*, 2025, **16**, 11012–11020.
27 X. Ji, S. Geng, S. Zhang, Y. Gong, X. Zhang, R. Li, Y. Liu, J. Chen, R. Chen, Z. Xiao and L. Mao, *Chem. Mater.*, 2022, **34**, 8262–8270.
28 T. Li, Y. Wang, Y. Liu, G. Liu, L. Meng, Y. Zheng and Y. Dang, *J. Mater. Chem. C*, 2025, **13**, 8238–8246.
29 X. Niu, Y. Li, H. Lu, Z. Wang, Y. Zhang, T. Shao, H. Wang, S. Gull, B. Sun, H. L. Zhang, Y. Chen, K. Wang, Y. Du and G. Long, *Nat. Commun.*, 2025, **16**, 2525.
30 J. Chen, X. Pan, X. Zhang, C. Sun, C. Chen, X. Ji, R. Chen and L. Mao, *Small*, 2023, 2300938.
31 C. Y. Chai, X. B. Han, C. D. Liu, C. C. Fan, B. D. Liang and W. Zhang, *J. Phys. Chem. Lett.*, 2023, **14**, 4063–4070.
32 D. Y. Liu, L. Y. Xiong, X. Y. Dong, Z. Han, H. L. Liu and S. Q. Zang, *Angew. Chem., Int. Ed.*, 2024, **63**, e202410416.
33 X. Yu, S. Zhong, Z. Guo, J. Guan, H. Tang, X. He, Y. Chen and S. Pan, *J. Mater. Chem. C*, 2025, **13**, 2190–2197.
34 M. Tao, R. Cao, S. Sun, H. Li and Y. Xiao, *Chem. Eur J.*, 2025, e202404470.
35 S. Wu, B. Zhou and D. Yan, *ACS Appl. Mater. Interfaces*, 2021, **13**, 26451–26460.
36 X. Dou, T. Zhu, Z. Wang, W. Sun, Y. Lai, K. Sui, Y. Tan, Y. Zhang and W. Z. Yuan, *Adv. Mater.*, 2020, **32**, 2004768.
37 J. You, X. Zhang, Q. Nan, K. Jin, J. Zhang, Y. Wang, C. Yin, Z. Yang and J. Zhang, *Nat. Commun.*, 2023, **14**, 4163.
38 C. Chen, Z. Luo, M. Zhang, X. Li, T. Zhang and J. Chen, *Dalton Trans.*, 2025, **54**, 12658–12666.
39 H. W. Lin, Y. P. Lin, D. D. Huang, Z. H. Chen, Y. C. Peng, Z. P. Wang, K. Z. Du and X. Y. Huang, *Inorg. Chem.*, 2023, **62**, 18331–18337.
40 H. W. Lin, A. Ablez, Z. H. Deng, Z. H. Chen, Y. C. Peng, Z. P. Wang, K. Z. Du and X. Y. Huang, *J. Mater. Chem. C*, 2024, **12**, 5184–5190.
41 R. Terki, G. Bertrand and H. Aourag, *Microelectron. Eng.*, 2005, **81**, 514.
42 R. W. Godby, M. Schlüter and L. J. Sham, *Phys. Rev. B*, 1987, **36**, 6497.
43 J. He, Y. Guo, W. Huang, X. Zhang, J. Yao, T. Zhai and F. Huang, *Inorg. Chem.*, 2018, **57**, 9918–9924.
44 H. Lin, B. X. Li, H. Chen, P. F. Liu, L. M. Wu, X. T. Wu and Q. L. Zhu, *Inorg. Chem. Front.*, 2018, **5**, 1458–1462.
45 T. E. Kokina, M. I. Rakhmanova, N. A. Shekhovtsov, L. A. Glinskaya, V. Y. Komarov, A. M. Agafontsev, A. Y. Baranov, P. E. Plyusnin, L. A. Sheludyakova, A. V. Tkachev and M. B. Bushuev, *Dalton Trans.*, 2020, **49**, 7552–7563.
46 R. X. Yuan, R. G. Xiong, Y. L. Xie, X. Z. You, S. M. Peng and G. H. Lee, *Inorg. Chem. Commun.*, 2001, **4**, 384–387.
47 X. G. Yang, X. M. Lu, Z. M. Zhai, J. H. Qin, X. H. Chang, M. L. Han, F. F. Li and L. F. Ma, *Inorg. Chem. Front.*, 2020, **7**, 2224–2230.
48 E. Najafi, M. M. Amini, P. Yousefi and S. W. Ng, *J. Inorg. Organomet. Polym. Mater.*, 2018, **28**, 1801–1809.
49 A. Dalal, A. Hooda, K. Nehra, D. Singh, S. Kumar, R. S. Malik and P. Kumar, *J. Mol. Struct.*, 2022, **1265**, 133343.
50 C. Zhang, S. Li, X. Y. Dong and S. Q. Zang, *Aggregate*, 2021, **2**, e48.
51 Q. Xu, J. Fu, M. Tang, H. Yao and J. Lin, *Adv. Opt. Mater.*, 2025, e01569.
52 J. C. Jin, N. N. Shen, Y. P. Lin, L. K. Gong, H. Y. Tong, K. Z. Du and X. Y. Huang, *Inorg. Chem.*, 2020, **59**, 13465–13472.
53 (*a*) CCDC 2488488: Experimental Crystal Structure Determination, 2026, DOI: 10.5517/ccdc.csd.cc2pjgtj; (*b*) CCDC 2488489: Experimental Crystal Structure Determination, 2026, DOI: 10.5517/ccdc.csd.cc2pjgvk.